# On New Method and 3D Codes for Shock Wave Simulation in Fluids and Solids in Euler Variables based on a Modified Godunov Scheme

M. H. ABUZIAROV, E. G. GLAZOVA, A. V. KOCHETKOV, S.V. KRYLOV
Research Institute for Mechanics,
Lobachevsly State University of Nizhni Novgorod,
RUSSIA

*Abstract:* A three-dimensional technique for modeling shock-wave processes both in fluids and solids and for modeling fluid-structure interaction problems is proposed. The technique is based on a modified Godunov's scheme of increased accuracy, which is the same for both fluids and solids, and uses Eulerian-Lagrangian multimesh algorithms. Improving the accuracy of the scheme is achieved only by changing the "predictor" step of the original Godunov scheme. A three-dimensional and time-dependent solution of Riemann's problem is used, which provides a second-order approximation in time and space in the domain of smooth solutions. Monotonicity in the domain of discontinuous solutions is ensured by the transition to the "predictor" step of the first-order scheme. A similar solution of the Riemann problem is used at the contact "fluids - solids". For each body, three types of computational grids are used with an explicit Lagrangian choice of movable free and contact surfaces. The first type of mesh used is a Lagrangian surface mesh in the form of a continuous set of triangles (STL file), which is used both to set the initial geometry of an object and to accompany it in the calculation process, and two types of volumetric three-dimensional meshes. These are the basic Cartesian fixed grid for each object, and auxiliary movable local Euler-Lagrangian grids associated with each triangle of the surface Lagrangian grid. The results of numerical simulation of the processes of the impact of ice fragments on a titanium plate, acceleration by detonation products of deformable elastoplastic bodies of various shapes, and steel strikers piercing an aluminum plate are presented.

*Key-Words:* - Godunov scheme, increased accuracy, Riemann problem, multimesh approach, 3D problems, detonation, elastic-plastic, hypoelastic, impact, penetration.

Received: December 8, 2022. Revised: October 15, 2023. Accepted: November 11, 2023. Published: December 14, 2023.

## 1 Introduction

Godunov scheme, [1], and its most famous modifications, [2], [3], [4], [5], [6], are widely used for solving nonlinear dynamic problems of fluid dynamics (CFD) in Eulerian variables due to the ability to distinguish and describe discontinuous solutions without artificial viscosity. At present, various modifications of this scheme are also used to solve problems of the dynamics of a deformable rigid body (CSD) in Eulerian and Eulerian-Lagrangian variables. The main problem of Godunov's scheme is the first order of approximation and, as a consequence, significant scheme viscosity, which leads to a fast decay of the solution. Numerous attempts to eliminate this drawback for CFDs, which are close in meaning to, [3], [4], [6], increase the difference stencil of the scheme and do not provide second-order accuracy in time in the domain of smooth solutions in the spatial case, and also create additional difficulties in the implementation of boundary conditions. In CSD, when modeling wave processes, the influence of the schematic viscosity is even more significant, and in many problems, it is necessary to use variants of the scheme with an approximation order of at least two. At present, for CSD, there are a large number of modifications of the Godunov scheme of increased accuracy, in particular, works, [7], [8], [9], [10], [11], [12], [13], [14], [15], [16], [17], [18], [19], [20]. In these works, modifications of the Godunov scheme of increased accuracy are developed, based on various versions of hyperelastic models of rigid body dynamics. These models are hyperbolic, invariant to the rotation of a rigid body, thermodynamically compatible, and can be written as a system of first-order differential equations in the form of conservation laws. The resulting modifications are laborious, are of more academic

interest, and have received limited distribution in computational practice and commercial packages. For hypoelastic CSD models, the solution to the problem of increasing the accuracy of numerical models was presented, [21], and further developed by him for various models of nonlinear material behavior in, [22]. It is shown that for hypoelastic models of media, including those describing irreversible deformations, and for "predictor-corrector" schemes with splitting into physical processes, it is sufficient at the "predictor" stage to obtain a solution of the linearized equations in the elastic approximation with the second order of accuracy. The nonlinear behavior of the material is taken into account at the "corrector" stage. In this case, the second order of approximation of the system of equations as a whole is preserved. In, [23], [24], a modification of Godunov's scheme for CSD of the second order of accuracy, monotonic on discontinuities was proposed. In this case, the exact solution of the Riemann problem in the elastic formulation is used for the linearized equations of the theory of plastic flow by the approach, [21], in a two-dimensional formulation on a compact stencil. This modification solved the problem of the increased scheme viscosity and the problem of boundary conditions. The increase in accuracy is achieved due to the convergence of the areas of influence of the differential and difference problems of the Riemann problem, the monotonicity of solutions in the area of discontinuities is ensured by the transition to the "predictor" of the scheme of the first order of accuracy. At the "fluid-elastic body" contact, the exact solution of the Riemann problem is also used. In, [25], [26], [27], [28], this modification was generalized to a three-dimensional case and three-dimensional problems of shock-wave loading of elastoplastic bodies were solved. Modeling three-dimensional dynamic processes of fluid-solid interaction (FSI) in Eulerian variables also requires an adequate description of complex processes at moving contact boundaries. Therefore, it is desirable to highlight and accompany the moving boundaries in the process of calculations. Currently, there are two approaches to describe the spatial motion of free and contact boundaries in Euler variables. The first approach is (the Sharp Interface Method - SIM), and the second is (the Diffusive Interface Method - DIM). The SIM approach, [29], [30], [31], [32], [33], [34], [35], [36], [37], involves precise selection and tracking of the motion of the boundary surface. The best option is the coincidence of the computational grid with the boundaries of the body, which is not always possible in the case of large displacements and deformations, and, in practice, is possible only in one-dimensional and two-dimensional cases. Variants associated with the use of various algorithms for tracking the location of the contact surface within moving or stationary Euler grids, often using the subgrid mesh technique to improve the accuracy in the most interesting parts of the computational domain (Adaptive Mesh Refinement technology -AMR), are also complex and are successfully applied only to solve two-dimensional problems. In the 3D case, this approach causes significant difficulties associated with tracking and restoring the surface of the bodies itself, dynamic non-Lagrangian rearrangement of meshes, and the implementation of boundary conditions. In, [35], a SIM approach for the 3D case using volume fractions and solving the Riemann problem of a "fluid-solid" discontinuity to restore and move the contact boundary inside cells with a mixture was proposed. The approach is conservative and includes AMR, but due to its complexity, it did not receive further development, even though it indicated the way to solve the problem. In, [36], also a SIM variant for the 3D case was proposed. The authors solve the Riemann problem inside cells with a mixture by interpolating and extrapolating parameters from the surrounding cells without a mixture to formulate and solve the Riemann problem. Then this solution is used to move the contact boundary inside the cells with the mixture and to calculate the fluxes to the surrounding cells, cutting them by the volume fractions in the cells with the mixture. Several procedures are iterative. Also, due to the complexity, the method did not find further development and application. The work, [38], is indicative in this respect, evolution from 2D SIM, [29], [30], [31], [32], [33], to 3D DIM, [38], [39]. It concludes the practical inapplicability of SIM for 3D problems. The second DIM approach, [40], [41], [42], [43], [44], [45], [46], [47], [48], [49], [50], [51], [52], [53], which is used on Eulerian grids, does not imply an exact selection of the contact surface and allows the use of cells containing mixtures of substances. With this approach, one has to construct an artificial non-physical equation of state for the mixture. Accordingly, it is necessary to construct a solution

for the Riemann problem for the Godunov-type schemes or special algorithms for determining fluxes and contact parameters for other schemes. In the most complicated versions, [39], [43], [44], a multi-component mixture with dynamic equilibrium is assumed in the cell, with possible sliding of the mixture components inside the cell — a multi-velocity continuum. This mixture must exhibit the properties of a deformable solid, passing continuously into a fluid or gas. The contact surface is not explicitly defined in this approach. This approach is convenient for solving 3D problems, but it has a significant numerical viscosity and does not have the required accuracy when describing complex contact phenomena such as friction, separation, cavitation, etc. In, [50], [51], similar approaches that have made it possible to solve several complex problems of the dynamic interaction of structural elements with gases in a 3D setting were developed. The multimesh approach proposed in, [25], [26], [27], [28], which is close in meaning to the gas dynamic numerical method "Chimera", [54], has no drawbacks associated with the difficulties in identifying and tracking contact surfaces and describing complex equations of state for dissimilar materials. This approach uses three types of computational meshes for each body and will be detailed below. The approach does not require complex three-dimensional mesh generators, it is enough to define the surfaces of bodies with STL files, which significantly speeds up the process of preparing data for calculation.

## 2 Governing Equations

The closed system of equations describing the deformation of a continuous medium in the approximation of a hypoelastic model of a compressible elastoplastic body in the Cartesian coordinate system has the following form, [21], [28]:

$$\rho_{,t} + \left(\rho u_i\right)_{,x_i} = 0 \tag{1}$$

$$\left(\rho u_i\right)_{,t} + \left(\rho u_i u_j - \sigma_{ij}\right)_{,x_j} = 0 \tag{2}$$

$$e_{,t} + \left(e u_j - u_i \sigma_{ij}\right)_{,x_j} = 0 \tag{3}$$

$$\mathrm{DS_{ij}}/\mathrm{Dt} + \lambda_t \mathrm{S_{ij}} = 2\mu e_{ij} \tag{4}$$

$$\varepsilon = \varepsilon(\mathrm{p},\rho), \tag{5}$$

Notation: t - time, $x_i$ - spatial coordinates, $u_i$ - components of the velocity vector along the axes $x_i$ respectively, $\rho$ - density, $e = \rho(\varepsilon + u_i u_i / 2)$ - total energy per unit volume, $\varepsilon$ - internal energy per unit mass, given by the equation of state (5), $\|\sigma_{ij}\|$ - which is represented as a ball and deviator parts, deviator of strain rate tensor $\sigma_{ij} = -p\delta_{ij} + S_{ij}$, $p = -\frac{1}{3}\sigma_{ii}$, $\|e_{ij}\|$ - deviator of strain rate tensor $e_{ij} = \varepsilon_{ij} - \frac{1}{3}\varepsilon_{kk}\delta_{ij}, where\ \varepsilon_{ij} = 1/2(u_{i,j} + u_{j,i})$. The symbol $\mathrm{D}/\mathrm{Dt}$ denotes the Yaumann derivative, which takes into account the rotation of the stress tensor in Euler variables. $\mathrm{DS_{ij}}/\mathrm{Dt} = S_{ij,t} + u_k \partial \mathrm{S_{ij}}/\partial \mathrm{x_k} - S_{ik}\omega_{jk} - S_{jk}\omega_{ik}$, where $\omega_{ij} = \frac{1}{2}(u_{i,j} - u_{j,i})$, $\mu$ - is the material shear modulus, and the index after the comma denotes differentiation concerning the corresponding variable (hypoelastic model). As a criterion for the transition from the elastic to the plastic state, the von Mises yield condition $S_{ij}S_{ij} = \frac{2}{3}\sigma_S^2$ under uniaxial tension is used, where $\sigma_S$ - the yield stress under uniaxial tension. The parameter $\lambda$ must remain positive during plastic deformation under the condition of fluidity $\lambda = \frac{3}{2}\frac{S_{ij}S_{ij}}{\sigma_S^2}$. The plastic flow is described by keeping the deviator on the surface of fluidity, [55]. The system of equations (1) – (5) is closed by equations of state with the corresponding parameters. In the absence of shear stresses, the system (1) – (5) goes over to the Euler equations for the motion of a compressible fluid or gas.

## 3 Second order Godunov Modification for CFD in Euler Variables on Compact Stencil

Assume all hydrodynamics parameters (primitive variables) to be linearly distributed in space between the cell centers for considered time steps. For example, for cell number i time step $t_n$ in X direction, vector function $U$ with scalar

components $p, \rho, u_1, u_2, u_3$ has the following distribution, Figure 1. In this section, index "I" defines the number of cells.

$$U(x) = U(x_{i-1}) + \frac{U(x_i) - U(x_{i-1})}{x_i - x_{i-1}}(x - x_{i-1}) \text{ if } x_{i-1} \le x \le x_i$$

$$U(x) = U(x_i) + \frac{U(x_{i+1}) - U(x_i)}{x_{i+1} - x_i}(x - x_i) \text{ if } x_i \le x \le x_{i+1}$$

Interpolating these primitive variables (for example, for cell number " i " with boundaries $x_{i-1/2}$ and $x_{i+1/2}$) into points $x_{i-1}^+, x_i^-$ - values $U(x_{i-1}^+), U(x_i^-)$ and into points $x_i^+, x_{i+1}^-$ - values $U(x_i^+), U(x_{i+1}^-)$ respectively.

Riemann problem is solved like in the original Godunov method (exact Riemann solution ) but for the cell's boundary $x_{i-1/2}$ between values $U(x_{i-1}^+)$ and $U(x_i^-)$ and for the boundary $x_{i+1/2}$ between values $U(x_i^+)$ and $U(x_{i+1}^-)$ respectively. For the original Godunov method, these Riemann problems are solved for the boundary $x_{i-1/2}$ between $U(x_{i-1})$ and $U(x_i)$ and for the boundary $x_{i+1/2}$ between values $U(x_i)$ and $U(x_{i+1})$ respectively. This is the main difference between this scheme and the original Godunov method. The coordinates of the points $x_{i-1}^+, x_i^- \; x_i^+, x_{i+1}^-$ are not known yet.

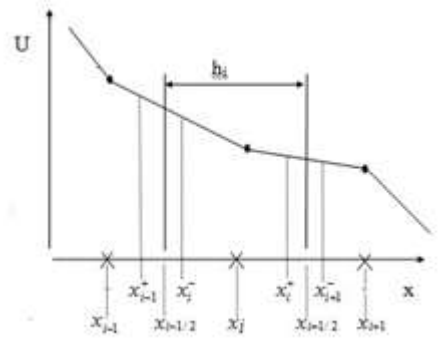


Fig. 1: Linear distribution of primitive parameters between cell centers

Flux calculation and the corrector step (integration) are the same as in the original Godunov method.

So now the integrated values at the time step $t_{n+1}$ are functions of primitive variables interpolated to these points $x_{i-1}^+, x_i^- \; x_i^+, x_{i+1}^-$. For linearized Euler equations, it is possible to solve the Riemann problem explicitly ( see APPENDIX 1 ) and obtain hydrodynamics parameters at the new time step as the explicit functions of coordinates of these points for interpolation of the primitive variables.

Let's try to use the appropriate selection of these points to optimize our numerical scheme (for example, to exclude or introduce the required viscosity terms). Let's analyze the one-dimensional linearized Euler equations (one-dimensional are considered only for simplicity, the analysis of three-dimensional cases is in, [56]):

$$u_t + u_0 * u_x + \frac{1}{\rho_0} * p_x = 0$$
$$p_t + u_0 * p_x + \rho_0 c_0^2 * u_x = 0, \tag{6}$$

where $p_0, \rho_0, u_0$ are points of linearization, $c_0 = c_0(p_0, \rho_0)$ sonic velocity, in our case as this point of linearization our integrating cell $p_i, \rho_i, u_i$ can be taken. Using formulas for the solution of the modified Riemann problem from APPENDIX 1 with expressions for interpolated values and for second order derivative of velocity in time from APPENDIX 2 for Godunov scheme formulas for these linearized Euler equations in APPENDIX 1, it follows from eq.6 the following modified equation:

$$u_t + u_0 * u_x * A_1 + \frac{1}{\rho_0} * p_x * B_1 =$$
$$= -\frac{u_{xx}}{2} * A_2 - \frac{p_{xx}}{2 * \rho_0 c_0} * B_2 + \bar{o}(h_i^2, \Delta t^2, \Delta t\, h_i)$$
$$p_t + u_0 * p_x * A_1 + \rho_0 c_0^2 * u_x * B_1 =$$
$$= -\frac{p_{xx}}{2} * A_2 - \frac{\rho_0 c_0 * u_{xx}}{2} * B_2 + \bar{o}(h_i^2, \Delta t^2, \Delta t\, h_i) \tag{7}$$

where $\Delta t = t_{n+1} - t_n$; $h_i = x_{i+1/2} - x_{i-1/2}$;
$h_{i-1} = x_{i-1/2} - x_{i-3/2}$; $h_{i+1} = x_{i+3/2} - x_{i+1/2}$

$$A_1 = \frac{1}{2h_i}\begin{pmatrix} x_i^+ + x_{i+1}^- - x_{i-1}^+ - x_{i-1}^- + \\ + c_0/u_0\left(x_i^+ - x_{i+1}^- + x_i^- - x_{i-1}^+\right) \end{pmatrix} \tag{8}$$

$$B_1 = \frac{1}{2h_i}\begin{pmatrix} x_i^+ + x_{i+1}^- - x_{i-1}^+ - x_{i-1}^- + \\ + u_0/c_0\left(x_i^+ - x_{i+1}^- + x_i^- - x_{i-1}^+\right) \end{pmatrix} \tag{9}$$

$$A_2 = \Delta t * (u_0^2 + u_0^2) + \\ + \frac{u_0}{2h_i}\begin{pmatrix}(h_{i-1}+h_i) * (x_{i-1}^+ + x_i^-) + \\ + (h_i + h_{i+1}) * (x_i^+ + x_{i+1}^-)\end{pmatrix}/2 + \\ + \frac{c_0}{2h_i}\begin{pmatrix}(h_{i-1}+h_i) * (x_{i-1}^+ - x_i^-) + \\ + (h_i + h_{i+1}) * (x_i^+ - x_{i+1}^-)\end{pmatrix}/2 \quad (10)$$

$$B_2 = 2u_0 c_0 \Delta t + \\ + \frac{u_0}{2h_i}\begin{pmatrix}(h_{i-1}+h_i) * (x_{i-1}^+ - x_i^-) + \\ + (h_i + h_{i+1}) * (x_i^+ - x_{i+1}^-)\end{pmatrix}/2 + \\ + \frac{c_0}{2h_i}\begin{pmatrix}(h_{i-1}+h_i) * (x_{i-1}^+ + x_i^-) + \\ + (h_i + h_{i+1}) * (x_i^+ + x_{i+1}^-)\end{pmatrix}/2 \quad (11)$$

So (7) are modified equations of (6) for our scheme and (7) have parameters to vary for obtaining a better scheme. The difference between (6) and (7) is the approximation error of our numerical scheme in simulating equations (6).

In formulas (8-11) coordinates $x_{i-1}^+, x_i^-$ and $x_i^+, x_{i+1}^-$ are taken relatively to $x_i$; this means $x_i = 0$. Further for simplicity $x_{i-1}^+, x_i^-$ are used relative to $x_{i-1/2}$ (relative to the border of the left cell), and $x_i^+, x_{i+1}^-$ are used relative to $x_{i+1/2}$ (relative to the border of the right cell's boundary) respectively. For system (6) to have an approximation error of the first order of accuracy, it is necessary that:

$$A_1 = 1 \; ; \quad B_1 = 1 \quad (12)$$

From eq. (6-9) and (12) it follows that:

$$x_{i-1}^+ = x_i^+ , \quad x_i^- = x_{i+1}^- \quad (13)$$

So choosing the interpolated points according to (13) is sufficient for first-order accuracy. Now the difference between (6) and (7) is only in the right terms (7). For system (6) to have the second order of accuracy, it is necessary in addition to (12) to have:

$$A_2 = 0; \; B_2 = 0 \quad (14)$$

Then it follows from (10 – 14) that:

$$x_{i-1}^+ = \left(\frac{\Delta t(-u_0 - c_0)}{2} + \frac{h_{i+1} - h_{i-1}}{8}\right) / \\ / \left(1 + \frac{h_{i+1} + h_{i-1} - 2h_i}{4h_i}\right); \qquad x_i^+ = x_{i-1}^+ \quad (15)$$

$$x_i^- = \left(\frac{\Delta t(-u_0 + c_0)}{2} + \frac{h_{i+1} - h_{i-1}}{8}\right) / \\ / \left(1 + \frac{h_{i+1} + h_{i-1} - 2h_i}{4h_i}\right); \qquad x_{i+1}^- = x_i^- \quad (16)$$

Formulas (15-16) determine the coordinates of such points, interpolation to which provides an approximation error of the second order of accuracy of system (6) for an irregular mesh for a given numerical method. For an irregular grid, it follows from (15-16) that the resulting scheme is not conservative, since the coordinates of these points are functions of the length of the integrating cell and its left and right neighbors. But for the commonly used uniform mesh or arithmetic progression mesh, where $h_i - h_{i-1} = h_{i+1} - h_i = \Delta$, it is conservative and formulas (15-16) take the following form:

$$x_{i-1}^+ = \left(\frac{\Delta t(-u_0 - c_0)}{2} + \frac{\Delta}{4}\right); \quad x_i^+ = x_{i-1}^+ \; ; \quad (17)$$

$$x_i^- = \left(\frac{\Delta t(-u_0 + c_0)}{2} + \frac{\Delta}{4}\right); \quad x_{i+1}^- = x_i^- \quad (18)$$

It is obvious from (17-18) that for an irregular mesh there is a displacement to a larger cell.

Thus, the second-order approximation error algorithm for the 1D linearized Euler equation is the following:

1. definition of coordinates of points $x_{i-1}^+, x_i^-$ and $x_i^+, x_{i+1}^-$ using formulas (15-16) or 17-18;
2. definition of $U(x_{i-1}^+)$ and $U(x_i^-)$ and $U(x_i^+)$ and $U(x_{i+1}^-)$ respectively (Figure 1);
3. solving the Riemann problems between $U(x_{i-1}^+)$ and $U(x_i^-)$ for boundary $x_{i-1/2}$ and between $U(x_i^+)$ and $U(x_{i+1}^-)$ for boundary $x_{i+1/2}$ respectively;
4. flux calculation and corrector step (integration) as in the original Godunov method.

Formulas (17) and (18) for obtaining the coordinates of interpolation points are very physical and have an obvious geometric interpretation. In

Figure 2 the coordinates of points $x_{i-1}^{+}$ and $x_i^{-}$ for the cell's boundary $x_{i-1/2}$ are presented. The zones of influence on the solution of the Riemann problem for this boundary of this cell at $\Delta t/2$ are restricted by these interpolation points. The total length of this zone is $c_0\Delta t$. All possible variants are presented in Figure 2. It is quite obvious that for this scheme there is no difference in the Riemann problem for the case of Lagrangian or Eulerian variables - there is always a Lagrangian choice of the solution, there is no analysis of the plane of characteristics. There is also no difference between subsonic and supersonic cases. The algorithm is obviously extended for the case of moving meshes – the interpolation coordinates are calculated like the zone of influence of the moving boundary or the coordinates of interpolation are calculated for the position of the boundary $x_{i-1/2}$ at time step level $\Delta t/2$. In other words, the coordinates of the zone of influence with the length $c_0\Delta t$ are calculated for the particle arriving at the boundary of the cell $x_{i-1/2}$ at the time step level $\Delta t/2$.

The "predictor" step of this scheme is practically the characteristics method for the time step level $\Delta t/2$ for the interpolated values. For acoustic equations for Courant number 1 for regular meshes for 1D case, it is the exact characteristics method for the predictor step and the scheme elaborated in this case is equivalent to the original Godunov method and has the same second-order accuracy. In general case choosing the interpolation points in the cell's centers changes this modification into the exact original Godunov method. Moving points of interpolation from values calculated by (17) or (18) one can introduce viscosity into this scheme, the value of this numerical viscosity can be regulated, by choosing the points of interpolation. The main advantage of this approach is that 3 cell stencil is enough for the second order accuracy, another very important thing – switching to the Riemann solution without interpolation (to the original Godunov method) provides the monotony of this modification on the same 3 cell stencil.

The algorithm for the exact second-order accuracy for linearized Euler equations in 2D, [57], and 3D, [56], cases is the following:

1. for each boundary of the cell it is assumed that the normal direction to the center of the surface of the boundary is X direction;
2. the coordinates of these interpolation points are the same as for the 1D case;
3. primitive variables at the cell's centers are to be corrected with the influence of the tangential gradients at $\Delta t/2$;
4. interpolation of these corrected primitive variables to appropriate points;
5. Riemann problem between these interpolated primitive variables;
6. calculation of the velocities tangential to the boundary surface (Riemann solver for tangential velocities) with the higher order accuracy at $\Delta t/2$ like in the Lax-Wendroff scheme;
7. flux calculation and integration as in the original Godunov's method.

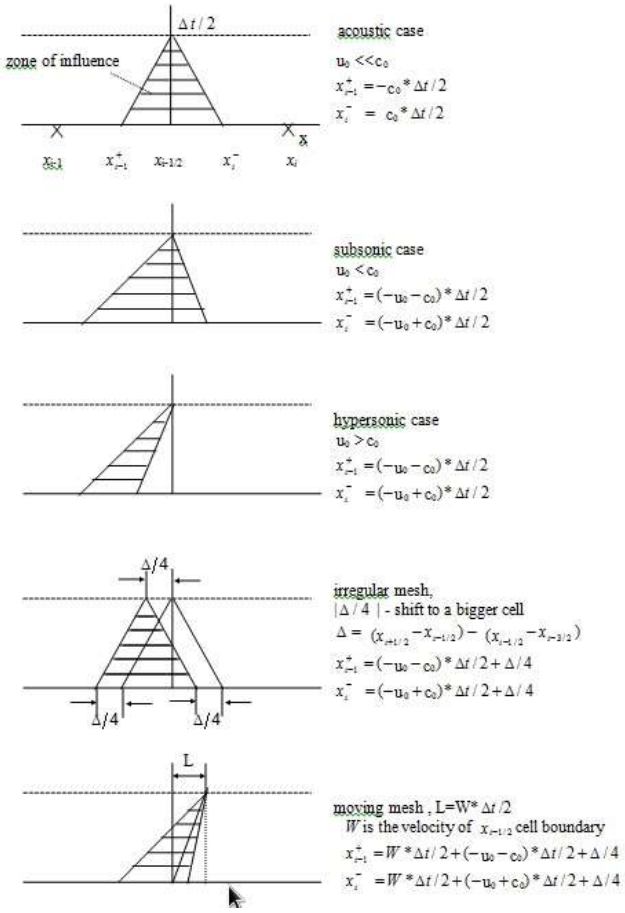


Fig. 2: Zone of influence on the Riemann solution at the cell boundary at $\Delta t/2$

The scheme obtained has second-order accuracy and it is not monotone. It is possible to introduce the numerical viscosity into this scheme moving the points of interpolation from values calculated by (17) and (18) (zero viscosity points) to the appropriate cell's centers – to the viscosity of the original Godunov scheme, which is enough for monotony. Analysis of the numerical results shows that the origin of nonmonotonicity is the big rate of the gradients. So the nonmonotonicity problems are coupled with the regions where the behavior of the solution mainly depends on the second-order derivatives. Physically these regions are at the top or the bottom of acoustic or shock waves, density discontinuities, and rarefaction waves. From the analysis of numerical results, obtained for this scheme, for the monotony of the numerical solution in such a problem-generating region it is enough to use the original Godunov predictor step for the one or two cell's boundaries. The main problem is how to detect such boundaries. It was suggested to use two parabolic splines, constructed from the primitive variables (pressure and density) in the vicinity of the analyzed cell's boundary, using three points. The two points of the centers of the cells, are used for the Riemann problem, and the nearest point to the left for the left spline and the nearest point to the right for the right spline. Such parabolic functions represent more precisely the behavior of numerical results. For example, these spline functions can be not monotone in these appropriate intervals when the numerical ones are still monotone. So these spline functions can be used even to predict the nonmonotone behavior of the numerical one. If the coordinate of the maximum or minimum of this spline function is not in appropriate interval it is possible to use Riemann solver for zero viscosity. The advantage of such spline function analysis is that it does not depend on the absolute values, only the analysis of the coordinate of maximum or minimum is enough for the choice of interpolation points. In the regions of constant solutions, the behavior of these spline functions does not have meaning for switching, because in these regions it does not matter to use a first or second-order Riemann problem solver. In the regions of smooth solutions or even in the regions of big gradients these spline functions are monotone, but when there are regions of big rates of gradients, these spline functions are not monotone.

# 4 Second-order Godunov Modification for CSD in Euler variables on Compact Stencil

In, [21], it was showed that for numerical modeling of dynamic elastoplastic equations with a second order of approximation for schemes of the "predictor-corrector" type at the "predictor" stage, it is sufficient to solve elastic equations $\lambda_t = 0$ with a second order of approximation using linearized equations (1) - (5 ). In this case, the plastic behavior of the medium is taken into account at the "corrector" stage after the integration of the linearized equations and is reduced to the "landing" of deviators on the yield surface, [21]. Let us denote $c^2 = (\partial p / \partial \rho)_s$; $f = \frac{1}{\rho(\partial \varepsilon / \partial p)_\rho}$, as a result, after linearizing the energy equation in the system of equations (1) - (5) and excluding the terms containing derivatives with respect to $x_2$ and $x_3$ (splitting in spatial variables is performed), we obtain a one-dimensional system of equations:

$$\rho_{,t} + u_1\rho_{,1} + \rho u_{1,1} = 0 \tag{19}$$

$$u_{1,t} + u_1u_{1,1} + 1/\rho * p_{,1} - 1/\rho * S_{11,1} = 0 \tag{20}$$

$$u_{2,t} + u_1u_{2,1} - 1/\rho * S_{12,1} = 0 \tag{21}$$

$$u_{3,t} + u_1u_{3,1} - 1/\rho * S_{13,1} = 0 \tag{22}$$

$$p_{,t} + (\rho c^2 - fS_{11})u_{1,1} - \\ - fS_{12}u_{2,1} - fS_{13}u_{3,1} + u_1p_{,1} = 0 \tag{23}$$

$$S_{11,t} - 4/3\mu u_{1,1} + S_{12}u_{2,1} + S_{13}u_{3,1} + u_1S_{11,1} = 0 \tag{24}$$

$$S_{22,t} + 2/3\mu u_{1,1} - S_{12}u_{2,1} + u_1S_{22,1} = 0 \tag{25}$$

$$S_{33,t} + 2/3\mu u_{1,1} - S_{13}u_{3,1} + u_1S_{33,1} = 0 \tag{26}$$

$$S_{12,t} - 0.5(2\mu + S_{11} - S_{22})u_{2,1} + 0.5S_{23}u_{3,1} + u_1S_{12,1} = 0 \tag{27}$$

$$S_{13,t} + 0.5S_{23}u_{2,1} - 0.5(2\mu + S_{11} - S_{33})u_{3,1} + u_1S_{13,1} = 0 \tag{28}$$

$$S_{23,t} - 0.5S_{13}u_{2,1} - 0.5S_{12}u_{3,1} + u_1S_{23,1} = 0 \tag{29}$$

In matrix form, equations (19-29) are:

$$\frac{\partial U}{\partial t} + A\frac{\partial U}{\partial x} = 0$$

where $U = [(\rho, u_1, u_2, u_3, p, S_{11}, S_{22}, S_{33}, S_{12}, S_{13}, S_{23})]$

$A =$

$$\begin{vmatrix}
u_1 & \rho & 0 & 0 & 0 & 0 & 0 & 0 & 0 & 0 & 0 \\
0 & u_1 & 0 & 0 & \frac{1}{\rho} & -\frac{1}{\rho} & 0 & 0 & 0 & 0 & 0 \\
0 & 0 & u_1 & 0 & 0 & 0 & 0 & 0 & -\frac{1}{\rho} & 0 & 0 \\
0 & 0 & 0 & u_1 & 0 & 0 & 0 & 0 & 0 & -\frac{1}{\rho} & 0 \\
0 & \rho c^2 - fS_{11} & -fS_{12} & -fS_{13} & u_1 & 0 & 0 & 0 & 0 & 0 & 0 \\
0 & -\frac{4}{3\mu} & S_{12} & S_{13} & 0 & u_1 & 0 & 0 & 0 & 0 & 0 \\
0 & \frac{2}{3\mu} & -S_{12} & 0 & 0 & 0 & u_1 & 0 & 0 & 0 & 0 \\
0 & \frac{2}{3\mu} & 0 & -S_{13} & 0 & 0 & 0 & u_1 & 0 & 0 & 0 \\
0 & 0 & \frac{S_{22}-S_{11}}{2}-\mu & 0.5S_{23} & 0 & 0 & 0 & 0 & u_1 & 0 & 0 \\
0 & 0 & 0.5S_{23} & \frac{S_{33}-S_{11}}{2}-\mu & 0 & 0 & 0 & 0 & 0 & u_1 & 0 \\
0 & 0 & -0.5S_{13} & -0.5S_{12} & 0 & 0 & 0 & 0 & 0 & 0 & u_1
\end{vmatrix}$$

In the case of constant coefficients of matrix A (linearized case), the system is hyperbolic and can be written in the form of 11 transport equations (in invariant form), [23], [24].

$$\frac{\partial R_l}{\partial t} + c_l \frac{\partial R_l}{\partial x} = 0,\ l = 1,\cdots,11,$$

Where $R_l$ are Riemann invariants constant for the corresponding characteristic velocity $c_l$. In the formulas below and Figure 3, the index "1" for the velocity $u_1$ and coordinate $x_1$ is omitted.

$$c_1 = u + a;\ c_2 = u - a;\ c_3 = u + \beta_y;\ c_4 = u - \beta_y;$$
$$c_5 = u + \beta_z;\ c_6 = u - \beta_z;\ c_7 = c_8 = c_9 = c_{10} = c_{11} = u;$$

Where $a^2 = c^2 + \frac{4/3\mu - fS_{11}}{\rho}$,

$$\beta_y = \sqrt{\frac{\mu + 3/4S_{11}}{\rho} - 0.5\sqrt{\frac{0.25*(S_{22}-S_{33})^2 + S_{23}^2}{\rho^2}}}$$

$$\beta_z = \sqrt{\frac{\mu + 3/4S_{11}}{\rho} + 0.5\sqrt{\frac{0.25*(S_{22}-S_{33})^2 + S_{23}^2}{\rho^2}}}$$

In the plane, $x_1, t$ the trajectories of discontinuities (characteristics) are depicted by rays emanating from the point x = $x_0$, and divide the half-plane t> 0 into 8 zones.

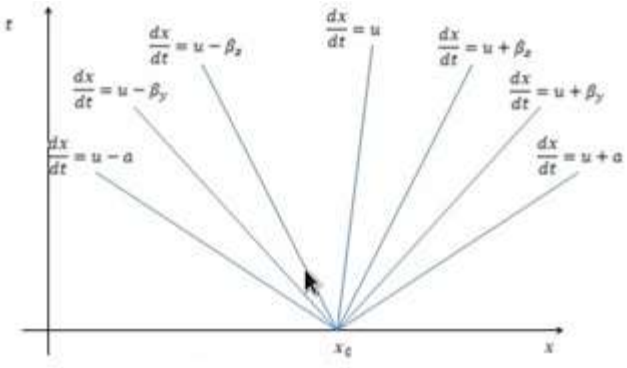


Fig. 3: Riemann solution zones for an elastic case, 1 order.

The ratios on these characteristics $R_l, l = 1,11$ have the following form:

$$R_1 = [\rho a]u_1 + p - S_{11} -$$
$$-\left[a(1+f)\frac{S_{12}(a^2-b_3^2) - S_{13}*0.5S_{23}/\rho}{(a^2-b_2^2)(a^2-b_3^2) - 0.25S_{23}^2/\rho^2}\right]u_2 -$$
$$-\left[a(1+f)\frac{S_{13}(a^2-b_2^2) - S_{12}*0.5S_{23}/\rho}{(a^2-b_2^2)(a^2-b_3^2) - 0.25S_{23}^2/\rho^2}\right]u_3 +$$
$$+\left[(1+f)\frac{\rho S_{12}(a^2-b_3^2) - S_{13}*0.5S_{23}}{\rho^2(a^2-b_2^2)(a^2-b_3^2) - 0.25S_{23}^2}\right]S_{12} +$$
$$+\left[(1+f)\frac{\rho S_{13}(\lambda^2-b_2^2) - S_{12}*0.5S_{23}}{\rho^2(a^2-b_2^2)(a^2-b_3^2) - 0.25S_{23}^2}\right]S_{13}$$

$$R_2 = [-\rho a]u_1 + p - S_{11} +$$
$$+\left[\rho a(1+f)\frac{\rho S_{12}(a^2-b_3^2) - S_{13}*0.5S_{23}}{\rho^2(a^2-b_2^2)(a^2-b_3^2) - 0.25S_{23}^2}\right]u_2 +$$
$$+\left[\rho a(1+f)\frac{\rho S_{13}(\lambda^2-b_2^2) - S_{12}*0.5S_{23}}{\rho^2(a^2-b_2^2)(a^2-b_3^2) - 0.25S_{23}^2}\right]u_3 +$$
$$+\left[(1+f)\frac{\rho S_{12}(a^2-b_3^2) - S_{13}*0.5S_{23}}{\rho^2(a^2-b_2^2)(a^2-b_3^2) - 0.25S_{23}^2}\right]S_{12} +$$
$$+\left[(1+f)\frac{\rho S_{13}(a^2-b_2^2) - S_{12}*0.5S_{23}}{\rho^2(a^2-b_2^2)(a^2-b_3^2) - 0.25S_{23}^2}\right]S_{13}$$

$$R_3 = [\beta_y\rho]u_2 - [\beta_y\rho C]u_3 - S_{12} + [C]S_{13}$$
$$R_4 = -[\beta_y\rho]u_2 + [\beta_y\rho C]u_3 - S_{12} + [C]S_{13}$$

where

$$b_2^2 = \frac{\mu + 0.5(S_{11} - S_{22})}{\rho};\ b_3^2 = \frac{\mu + 0.5(S_{11} - S_{33})}{\rho}$$

$$R_5 = [\beta_z\rho C]u_2 - [\beta_z\rho]u_3 - [C]S_{12} + S_{13}$$

where $C = \sqrt{1 - \frac{2}{1 + \sqrt{1 + \frac{4S_{23}^{\ 2}}{(S_{22} - S_{33})^2}}}}$; $0 \le C \le 1$

$$R_6 = -[\beta_z \rho C]u_2 + [\beta_z \rho]u_3 - CS_{12} + S_{13}$$

$$R_7 = [a^2]\rho - p + S_{11} +$$
$$+\left[\frac{(1+f)(S_{12}\rho b_3^{\ 2} + 0.5S_{23}S_{13})}{\rho b_2^{\ 2}\rho b_3^{\ 2} - 0.25S_{23}^{\ 2}}\right]S_{12} +$$
$$+\left[\frac{(1+f)(\rho b_2^{\ 2}S_{13} + 0.5S_{23}S_{12})}{\rho b_2^{\ 2}\rho b_3^{\ 2} - 0.25S_{23}^{\ 2}}\right]S_{13}$$

$$R_8 = \left[4/3\frac{\mu}{\rho}\right]\rho + S_{11} +$$
$$+\left[\frac{S_{12}\rho b_3^{\ 2} + 0.5S_{23}S_{13}}{\rho b_2^{\ 2}\rho b_3^{\ 2} - 0.25S_{23}^{\ 2}}\right]S_{12} +$$
$$+\left[\frac{\rho b_2^{\ 2}S_{13} + 0.5S_{23}S_{12}}{\rho b_2^{\ 2}\rho b_3^{\ 2} - 0.25S_{23}^{\ 2}}\right]S_{13}$$

$$R_9 = \left[-2/3\frac{\mu}{\rho}\right]\rho + S_{22} +$$
$$+\left[\frac{-S_{12}\rho b_3^{\ 2}}{\rho b_2^{\ 2}\rho b_3^{\ 2} - 0.25S_{23}^{\ 2}}\right]S_{12} +$$
$$+\left[\frac{-0.5S_{23}S_{12}}{\rho b_2^{\ 2}\rho b_3^{\ 2} - 0.25S_{23}^{\ 2}}\right]S_{13}$$

$$R_{10} = \left[-2/3\frac{\mu}{\rho}\right]\rho + S_{33} +$$
$$+\left[\frac{-0.5S_{23}S_{13}}{\rho b_2^{\ 2}\rho b_3^{\ 2} - 0.25S_{23}^{\ 2}}\right]S_{12} +$$
$$+\left[\frac{-\rho b_2^{\ 2}S_{13}}{\rho b_2^{\ 2}\rho b_3^{\ 2} - 0.25S_{23}^{\ 2}}\right]S_{13}$$

$$R_{11} = \left[\frac{-0.5S_{13}\rho b_3^{\ 2} - 0.25S_{23}S_{12}}{\rho b_2^{\ 2}\rho b_3^{\ 2} - 0.25S_{23}^{\ 2}}\right]S_{12} +$$
$$+\left[\frac{-0.5\rho b_2^{\ 2}S_{12} - 0.25S_{23}S_{13}}{\rho b_2^{\ 2}\rho b_3^{\ 2} - 0.25S_{23}^{\ 2}}\right]S_{13} + S_{23}$$

Here, the values in square brackets are the linearization coefficients determined from the averaged parameters in the cells. For a scheme of the first order of accuracy, for the zone where the solution is sought (where the corresponding face of the cell is located), the corresponding invariants are determined and the primitive parameters necessary for calculating the fluxes are determined from them. For a second-order accurate scheme, in contrast to the equations of gas dynamics, the Riemann invariants, [23], [24] obtained from primitive parameters are interpolated from the centers of the cells and are to be corrected with the influence of the tangential gradients at $\Delta t/2$. The coordinates of the interpolation points are determined as the boundaries of the areas of influence of the corresponding invariants on the position of the boundary face at the time $\Delta t/2$, where $w$ edge velocity (indicated by a dotted line in Figure 4) is as follows: $x_n = \frac{(x_{i-1} + x_i)}{2} - (c_n - w)\frac{\Delta t}{2}$, $n = 1,..,11$ ,

where

$c_1 = u + a$; $c_2 = u - a$; $c_3 = u + \beta_y$; $c_4 = u - \beta_y$;

$c_5 = u + \beta_z$; $c_6 = u - \beta_z$; $c_7 = c_8 = c_9 = c_{10} = c_{11} = u$;

Let us denote the interpolated invariants by the index "$m$", respectively

$$R_n^m = R_n^{i-1} + \frac{R_n^i - R_n^{i-1}}{x_i - x_{i-1}}(x_n - x_{i-1}),\ n = 1,..,11 \cdot$$

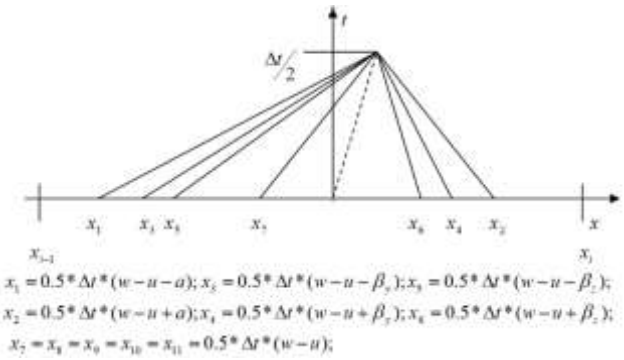


Fig. 4: The coordinates of interpolation points of Riemann invariants for a second-order accurate scheme

The obtained values of the Riemann invariants are used to determine the primitive parameters and "stream" values. The stage of numerical integration of the equations ("corrector" step) remains unchanged (as for the first-order scheme by, [21]). The solution according to the second-order scheme will experience dispersive oscillations at the discontinuities. To ensure monotonicity, it is necessary to construct the solution in a hybrid manner - in the regions of smoothness according to the relations providing the second order of approximation, and on discontinuities - according to the relations of the first order scheme. For elastoplastic flows, in contrast to the problems of gas dynamics, where it is necessary to analyze the pressure and density fields, to obtain monotonic solutions, it is sufficient to analyze the normal stress

field and use the obtained viscosity as a relative one to determine the interpolation coordinates of the remaining invariants, [23], [24].

## 5 Riemann Solver for FSI

The solution of the contact problem between fluid and solid is realized at the "predictor" stage of the Godunov scheme (at the stage of solving the Riemann problem). From the side of the deformable body, 8 invariants arrive at the boundary and 3 boundary conditions are used. On the fluid side, three relationships are used for nonlinear compression and rarefaction waves. To improve the accuracy in the domain of smooth solutions, extrapolation of parameters from the boundary and boundary cells is used. An iterative algorithm for obtaining a joint solution, in the general case, looks like this:

1. for the fluid parameters, boundary conditions of the movable "rigid wall" type are realized, the normal velocity of which is equal to the velocity in the adjoining cell of the deformable body; as a result, we obtain the pressure at the "fluid - deformable body" interface.
2. for obtaining the parameters of the boundary cell of a deformable body, the following equations are used: Riemann invariants number 1,3,5,7,8,9,10,11 are taken from the center of the boundary cell, possibly with interpolation from inside the body to improve accuracy, instead of the Riemann invariant number 2 the normal stress equal to pressure with the opposite sign, obtained in item 1, is used, and instead of Riemann invariants number 4 and 6 - zero tangential stresses or stresses taking into account friction are used.
3. The new normal boundary speed defined in item 2 is used cyclically in item 1 as the normal velocity of the rigid wall. The process continues until the convergence of this normal velocity. As a rule, 3-4 iterations are sufficient until convergence with a relative accuracy of 0.01.

## 6 Multimesh SIM for 3D Nonmoving Euler Mesh

This SIM approach is multimesh and uses three types of computational meshes, [25]. The first type of meshes is Lagrangian meshes in the form of STL files that define and accompany the deforming surfaces of bodies. Fixed regular Euler meshes with cubic cells are used inside homogeneous regions. The third type of grid is auxiliary local movable Euler-Lagrangian meshes associated with the surfaces of bodies. In general, the algorithm for calculating the contact interaction of fluids and solids in nonmoving Euler consists of a sequence of the following steps:

1) Fluids and solids are specified in the form of surfaces from sets of triangles with the required precision - in the form of STL files containing external normals and coordinates of triangle vertices. In Figure 5 such objects are marked in red and blue.

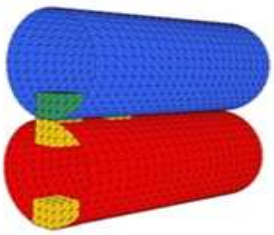

Fig. 5: STL surfaces of touching objects and local meshes

2) Each computational domain (fluid, solid) with curved boundaries is enclosed in a bordering rectangular parallelepiped and covered with a Cartesian mesh. Figure 6 shows a cross-section of such a computational domain (black solid curve) with a bordering parallelepiped. We get four types of cells for the computational domain, the first type - cells cut by triangles of the surface or boundary cells, are colored green, the second type - is cells outside the surface, the third and fourth types - are cells inside the surface, for which there are enough (brown) or not enough to integrate (marked with black dots) of a difference stencil of whole cells located inside the surface.

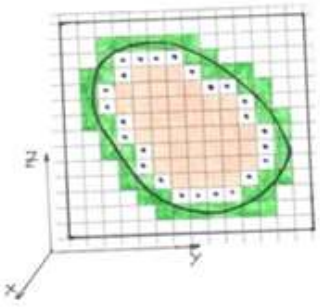


Fig. 6: Cross-section of the 3D computational domain

3) On each triangle of the surface, inside the volume along the normal for this surface, an auxiliary local Cartesian grid 3 * 3 * 3 is built , in Figure 5 these meshes are yellow. The cell sizes of this local three-dimensional mesh are taken close to the cell sizes of the inner mesh. In case of contact with another subdomain or boundary conditions that require additional parameters, the local mesh is symmetrically completed in this subarea from the plane of the triangle, in Figure 5 this completed mesh is marked in green. Figure 7 shows this auxiliary mesh for one triangle.

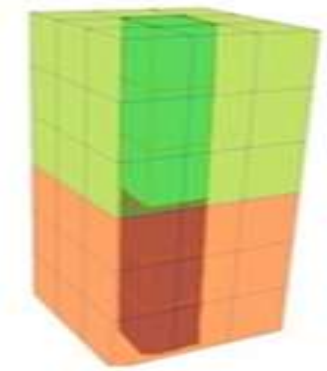

Fig. 7: Local mesh for one triangle of STL mesh

Figure 8 shows one triangle and the adjacent central cells of the auxiliary mesh, the centers of the edges of these cells coincide with the center of the triangle.

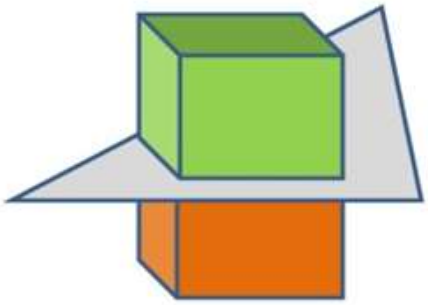

Fig. 8. Triangle and two adjacent cells of the local mesh.

Parameter values in the generated local mesh are determined by interpolation of parameters from the previous local mesh and parameters from the main mesh. This stencil is sufficient to integrate the central cells (in Figure 7 it is highlighted in dark and in Figure 9 these cells are shown separately and marked with crosses) adjacent to the Lagrangian contact surface, with increased accuracy according to the modified Godunov scheme. For the central cells from Figure 8, the Riemann problem at the contact boundaries of the media is solved. Its solution results in velocities and forces at a half-time level in the center of the corresponding triangle. We move this contact boundary with normal speed and get a local mesh on a new time layer. Figure 9 shows these center cells before (left side) and after moving the contact boundary (right side). We carry out the standard integration of the parameters of these central cells in movable meshes (ALE integration). Since the motion of the local grid is one-dimensional, the volume and surface integrals over the cells are calculated exactly in this case.

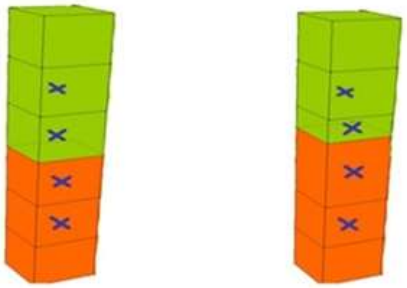

Fig. 9: Central cells before and after integration with the motion of the contact boundary in the normal direction (ALE integration).

4) Using the velocities in the center of each triangle obtained from solving the Riemann problem in step 3), we calculate the velocities at the vertices of the triangles in the STL file with weights proportional to the areas of the triangles. With these speeds, we move the vertices and get the position of the surface on a new time layer (the new position of the STL file).

5) We rebuild the bordering parallelepiped with the possible addition or reduction of layers of cells by the new position of the STL file. The cross-section of this surface with a bordering parallelepiped is shown in Figure 10. The red curve corresponds to the position of the computational domain on the new time layer. To the cells of the fourth type, which remained in the computational domain on a new temporary layer (marked with crosses on a white background), add non-integrated

cells captured during surface movement (marked with crosses on a green background).

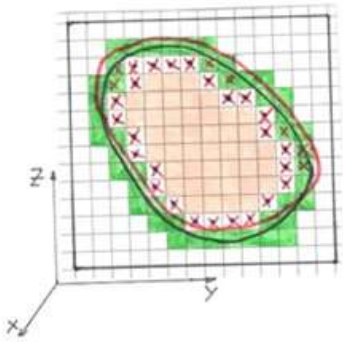

Fig. 10: New STL surface position with additional non-integrated cells.

6) In the cells of the fourth type (marked with crosses on a white and green background), we interpolate the parameters from the integrated cells of the third type and the integrated cells of the local meshes, thus completing the calculations.

## 7 Modeling the Interaction of Ice Impactors with a Clamped Titanium Plate

The problem statement is shown in Figure 11. An ice ball on the left and a cylinder on the right hit the titanium plate. It is required to describe in a coupled formulation the processes of interaction of ice projectiles with an elastoplastic deformable plate. Plate dimensions from the origin (embedment plane): length along the X-axis 150 mm, width along the Y-axis 50 mm, height along the Z-axis 5 mm, the plate is rigidly fixed in the plane X = 0, material - VT6 titanium, [58], with mechanical characteristics: density 4.51 g/cm3, the bulk compression modulus is 112 GPa, the shear modulus is 41GPa, yield strength 1.45 GPa. At the moment of impact, the coordinates of the point of contact between the ball and the axis of symmetry of the cylinder are X = 134 mm, Y = 25 mm, and Z = 5 mm. An ice ball has a diameter of 28 mm, a cylinder - diameter of 17.1 mm, height of 50 mm; weights are the same as 10.35 g, mechanical characteristics of ice: density 0.9g / cm3, the bulk compression modulus is 9.196 GPa, the shear modulus is 3.5263 GPa, yield point 5.2 MPa. The initial vertical velocity of the impacters in both cases is 350 m/s. At the outer boundaries of the metal barrier and ice impacters, the conditions are fulfilled as at the “free boundary” with a given pressure p = 0.1 MPa. The dimensions of the cells along the ice and the obstacle were taken 0.5 mm, which required about six hundred thousand cells of the main grid. In the process of impact, the hailston and the plate undergo significant displacements and deformations, and the destruction of the hailston occurs. Figure 12 and Figure 13 also show the positions of the bodies and the computational mesh in the longitudinal plane of symmetry along the ball and cylinder at an instant of 800 μs. Figure 14 shows the velocities of the plate versus time on the axis of symmetry of the sphere, marked in red, and of the cylinder, marked in green, from the beginning of the interaction to 120 μs. Figure 15 shows the same parameters from the beginning of the interaction to 800 μs. The difference in the initial moment is due to the larger initial interaction area for a cylindrical object. In the process of interaction, the strikers spread out over the plate, completely losing their shape, and starting from the moment of 120 μs, the influence of the initial geometry ceases to affect the movement of the plate.

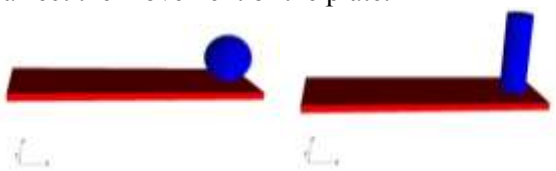

Fig. 11: Initial position of impactor and plate

Fig. 12: Shapes of objects 800 μs after impact

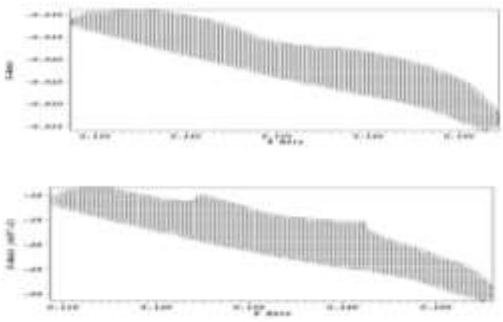

Fig. 13: Computational mesh for spherical and cylindrical impactors, a cross-section along the X axis, 800 μs after impact

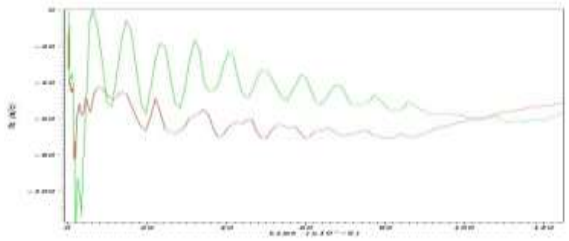

Fig. 14: The vertical velocity of the plate at the point of impact versus time, red for the ball, green for the cylinder (0-120 μs)

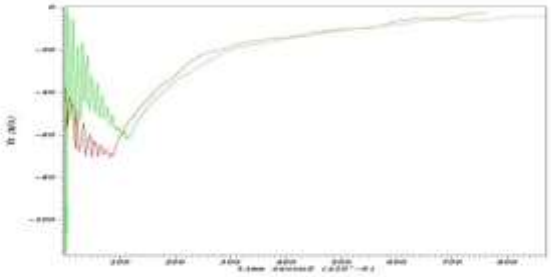

Fig. 15: The vertical velocity of the plate at the point of impact versus time, red for the ball, green for the cylinder (0-800 μs)

## 8 Interaction of Elastic-Plastic Bodies with the Product of Detonation

In Figure 16 the statement of the problem is given. Charge of TNT-RDX TR 8530 of the spherical shape, radius 5 cm, the source of initial detonation was set in a region of radius less than 0.2 cm. The cross-section passes through the center of the charge and the centers of the cubes. In the charge and the air, the main mesh was used with the side of the cubic cell 0.15 cm. For the explosive, the parameters of the equation of state of the JWL type are taken from, [13], as A=708.6056 GPa, B=13.16457 GPa, C=1.058238 GPa, $r_1$=4.94, $r_2$=1.35, $\omega$=0.28. The same state equation is used for air, air is assumed like the product of detonation for Euler simulation without tracking the interface "detonation product" – "air". Three steel cubes with sides 1 cm are marked with red color, the density is 7.8 g/cm$^3$, the bulk compression modulus is 175 GPa, the shear modulus is 80.77 GPa, the hardening modulus is 240 MPa, and the yield strength is 340 MPa, weight 7.8 grams. The step of the main grid in cubes is 0.7 mm. In Figure 16 the grids for steel and TNT are given. In Figure 17 the density distribution is presented at the moment of 55 μs. The cubes are strongly and irreversibly deformed, the streams of detonation products move much faster, and gas jets are formed around the cubes. In Figure 18 the shape of the cubes, respectively, at the initial moment and for 13 and 55 μs. By 13 μs the fragments practically acquired a residual form by slightly changing their position. Figure 19 shows the velocity versus time on the surface of the cube, accelerated in the vertical direction, the lower curve corresponds to the center of the upper surface (far from the charge), respectively, the upper curve - to the center of the lower surface of the cube (near to the charge). Figure 20 shows the velocity of the center of mass versus time for the cube, accelerated in the vertical direction, marked by "1" and for the cube, accelerated in a 45-degree direction, marked by "2". Dashed lines indicate these dependencies, calculated in an elastic formulation. Taking into account the plastic deformation of the bodies increases the maximum velocity of the body by more than 20 percent. The maximum velocity of a body strongly depends on its shape and position relative to the surface of the charge.

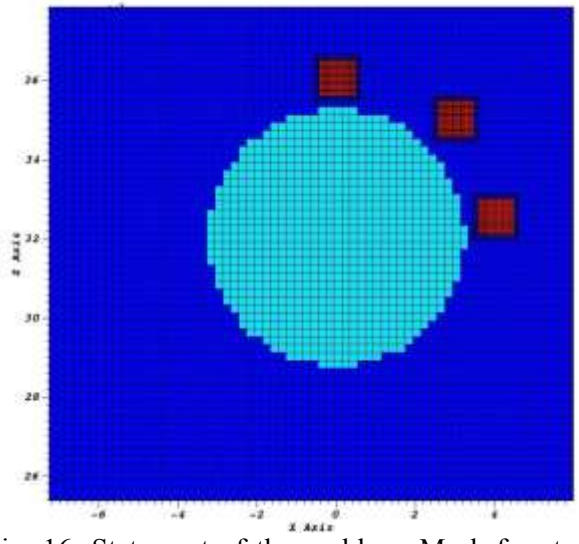

Fig. 16: Statement of the problem. Mesh for steel, TNT, and air

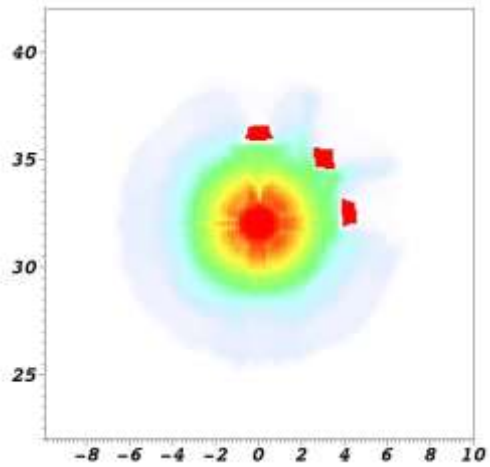


Fig. 17: Density distribution at 55 μs

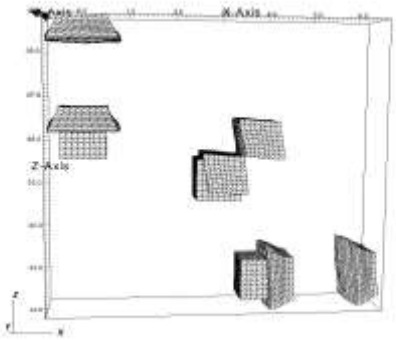

Fig. 18: Shape of the cubes, respectively, at the initial moment, at 13 and 55 μs

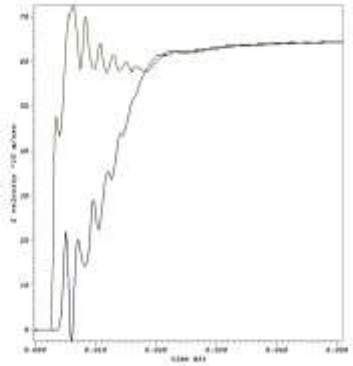

Fig. 19: Velocity versus time on the bottom and top of the cube

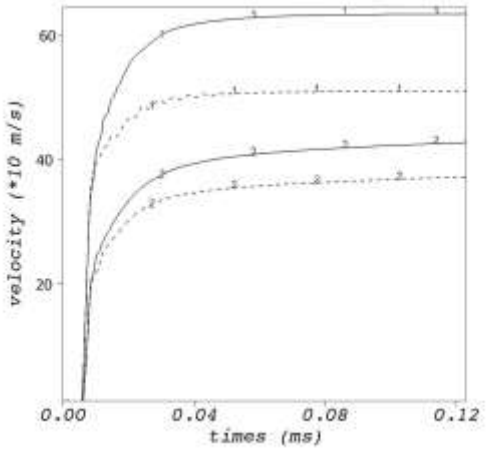


Fig. 20: Velocity of the center of mass versus time, initial positions in vertical and 45-degrees. Dashed lines show the calculations of the elastic setting.

## 9 Perforation of Aluminum Plate with Ogive Nose Steel Rod at Oblique Impact

Figure 21 shows the formulation of the problem of punching with a steel impactor, velocity of 400 m / s, with an aluminum plate, [59], at an angle of 30 degrees. The surfaces (STL files) of the impactor and target are shown in detail in Figure 22. Steel, the density is 7.85 g/cm3, the bulk compression modulus is 175 GPa, the shear modulus is 80.77 GPa, the yield strength is 3.4 GPa and the hardening modulus is 2.4 GPa. Aluminum, the density is 2.71 g/cm3, the bulk compression modulus is 67.64 GPa, the shear modulus is 26 GPa, the ideal plasticity, and the yield strength is 0.262 GPa. The dimensions of the main mesh in both bodies are 0.01 cm In the experiment, [59], the plate is 55x55x2.63 cm; in the calculations, the slab of smaller dimensions is 10x10x2.63 cm with free boundaries, rests along the perimeter on a rigid frame (Figure 23) with a width of 1 cm. In Figure 24 and Figure 25, there are computational grids at 200 and 540 μs, respectively. Figure 26 shows the punched plate in the direction of the initial velocity vector of the impactor at the moment of 540 μs. The Figure 27 shows the shapes of the striker at the moment of 40 μs, with a deflection with a tendency to ricochet, and at the moment of departure 540 μs with the opposite deflection, which was noted in experiments, [59]. The numerical values of the residual velocity of the impactor vary in the range from 195 to 205 m / s

due to elastic vibrations, which is close to the measured average values - 200 m / s, [59].

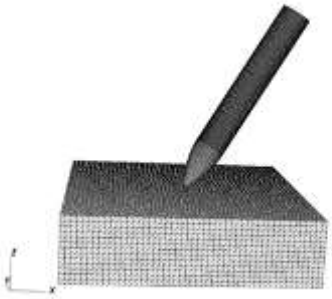

Fig. 21: Oblique impact, rod velocity 400 m/s. STL surfaces

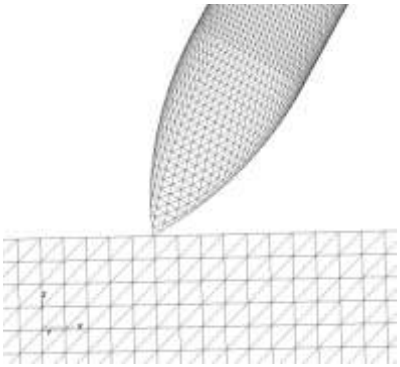

Fig. 22: Part of STL surfaces

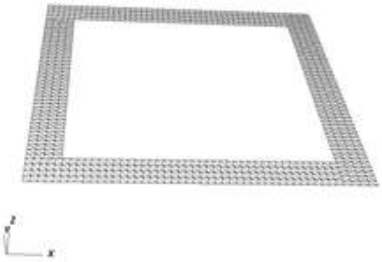

Fig. 23: Rigid frame supporting the aluminum plate

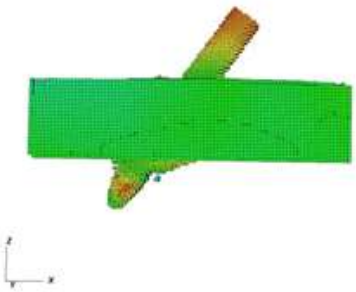

Fig. 24: Computational mesh at 200 μs

Fig. 25: Computational mesh at 540 μs

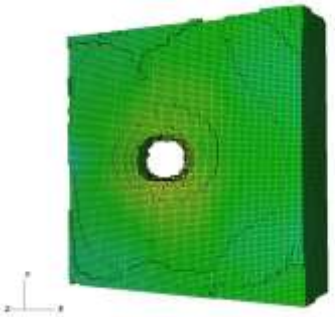

Fig. 26: Perforated aluminum plate at 540 μs

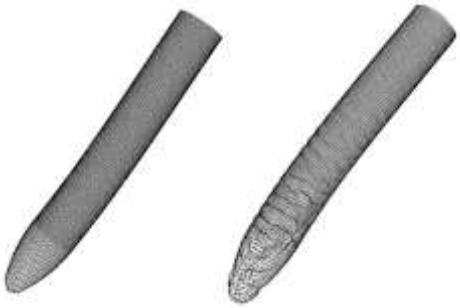

Fig. 27: Steel rod at 40 and 540 μs (STL surfaces)

## 10 Conclusions

The multimesh numerical technique developed and described in this article for solving three-dimensional problems of propagation of wave processes in fluids and solids and the interaction of the fluid with elastoplastic deformable bodies at large displacements and deformations allows obtaining reliable results with sufficiently high accuracy. The results of numerical studies are in good agreement with the known experimental data. The use of STL files for constructing all types of meshes and describing the motion of Lagrangian

contact and boundary surfaces within the framework of this multimesh approach, as well as the use of regular fixed Euler mesh, makes it possible to dramatically simplify the preparation of initial data for solving complex problems and to increase the efficiency and accuracy of calculations by eliminating distortions and rebuilding of computational meshes in traditional Euler-Lagrangian techniques.

*Acknowledgments:*
This work has been supported by the grants of the Russian Science Foundation, RSF 22-79-10076.

*References:*

[1] Godunov S.K.. A finite difference method for the computation of discontinuous solutions of the equations of fluid dynamics. *Math.Sbornik,* Vol.47, 1959, pp.271–306.

[2] S.K. Godunov, A.V. Zabrodin, and G.P. Prokopov. A difference scheme for two-dimensional nonstationary fluid dynamics problems and flow with a bow shock wave, *Zh. Vychisl. Mat. Mat. Fiz*. Vol. 1, 1961, pp.1020–1050.

[3] V.P. Kolgan. Application of the minimum derivative principle for constructing finite difference schemes for the calculation of discontinuous solutions in fluid dynamics, *Uchen. Zapiski of TsAGI* Vol.3, No.6, 1972, pp.68–77.

[4] B. Van Leer, Towards. The ultimate conservative difference scheme V: A second-order sequel to Godunov's method, *J. Comput. Phys*. Vol.32, 1979, pp. 101–136.

[5] P.L. Roe. Approximate Riemann solvers, parameter vectors and difference schemes, *Journal of Computational Physics*, Vol. 43, 1981, pp.357-372.

[6] P. Colella and P.R. Woodward. The piecewise-parabolic method (PPM) for gas-dynamics simulations, *J. Comput. Phys.*Vol. 54, 1984, pp.174–201.

[7] Hill D.J., Pullin D., Ortiz M., Meiron D.. An Eulerian hybrid WENO centered-difference solver for elastic–plastic solids, *Journal of Computational Physics*. Vol. 229, 2010, pp. 9053–9072.

[8] Trangenstein J.A., Colella P.. A higher-order Godunov method for modeling finite deformation in elastic–plastic solids, *Commun. Pure Appl. Math.* Vol. 44, 1991, pp. 41–100.

[9] Miller G.H., Colella P.. A high-order Eulerian Godunov method for elastic-plastic flow in solids, *J. Comput. Phys.,* Vol. 167, 2001, pp. 131–176.

[10] Gavrilyuk S.L., Favrie N., Saurel R.. Modelling wave dynamics of compressible elastic materials, *J. Comput. Phys.* Vol. 227, 2008, pp. 2941–2969.

[11] Favrie N., Gavrilyuk S.L.. Dynamics of shock waves in elastic–plastic solids, in: *ESAIM Proceedings.* 2010, pp. 1–18.

[12] Dumbser M., Peshkov I., Romenski E., Zanotti O. High order ADER schemes for a unified first order hyperbolic formulation of continuum mechanics: viscous heat-conducting fluids and elastic solids, *J. Comput. Phys*. Vol. 314, 2016, pp. 824–862.

[13] Barton P.T., Drikakis D., Romenski E., Titarev V.A. Exact and approximate solutions of Riemann problems in non-linear elasticity, *J. Comput. Phys*. Vol. 228, 2009, pp. 7046–7068.

[14] Barton P., Romenski E. On computational modelling of strain-hardening material dynamics, *Commun. Comput. Phys*. Vol.11, 2012, pp. 1525–1546.

[15] Menshov I., Mischenko A., Serezkin A. Numerical modeling of elastoplastic flows by the Godunov method on moving Eulerian grids. *J. Mathematical Models and Computer Simulations*, Vol. 6, No. 2, 2013, pp. 127-135.

[16] Barton P.T., Drikakis D. An Eulerian method for multi-component problems in non-linear elasticity with sliding interfaces, *J. Cornput, Phys.* Vol.229, No. 15, 2010, pp. 5518-5540.

[17] Barton P.T., Drikakis D., Romenski E. An Eulerian finite-volume scheme for large elastoplastic deformations in solids, *Int. J. Numer. Methods Eng*. Vol. 81, 2010, pp. 453-461.

[18] A.López Ortega, Lombardini M., Pullin D.I., Meiron D.I. Numerical simulation of elastic-plastic solid mechanics using an Eulerian stretch tensor approach and HLLD Riemann solver, *J. Comput. Phys*. Vol. 257, 2014, pp. 414–441.

[19] Schoch S., Nordin-Bates K., Nikiforakis N. An Eulerian algorithm for coupled simulations of elastoplastic-solids and condensed-phase explosives, *J.Com-put. Phys*. Vol. 252, 2013, pp. 163–194.

[20] Titarev V.A., Romenski E., Toro E.F. MUSTA-type upwind fluxes for non-linear elasticity, *Int. J. Numer. Methods* Eng. Vol. 73, 2008, pp. 897-911.

[21] Kukudzhanov V.N. Decomposition method for elastoplastic equations *Mech. Solids* Vol. 39, No. 1, 2004, pp. 73–80.

[22] Kukudzhanov V. N., Coupled models of elastoplasticity and damage and their integration, *Mechanics of Solids* Vol. 41, No. 6, 2006, pp. 83–109.

[23] Abouziarov M., Aiso H., Takahashi T. An application of conservative scheme to structure problems, *Series from Research Institute of Mathematics of Kyoto University. Mathematical Analysis in Fluid and Gas Dynamics*. No. 1353, 2004, pp. 192-201.

[24] Abouziarov M.X., Aiso H. An application of retroactive characteristic method to conservative scheme for structure problems (elastic-plastic flows), *Hyperbolic Problems, Theories, Numerics, Applications. Tenth International Conference in Osaka. September 2004, Copyright 2006 by Yokohama Publishers, Inc.,* pp. 223-230.

[25] Abuziarov K.M., Abuziarov M.H., Kochetkov A.V. 3d fluid-structure interaction problem solving method in Euler variables based on the modified Godunov scheme, *Materials Physics and Mechanics*. Vol.28, No.1-2, 2016, pp. 1-5.

[26] Abuziarov K.M. The method of decomposition of gapes in the three-dimensional dynamics of elastoplastic media. *Problems of Strength and Plasticity*. Vol. 82. No 3, 2020, pp. 5-17.

[27] K.M. Abuziarov, M. Abuziarov, E.G. Glazova, A.V. Kochetkov, S.V. Krylov, E.E. Maslov, B.I. Romanov. Numerically modeling 3d processes of explosive acceleration of elastoplastic bodies. *Problems of Strength and Plasticity.* Vol. 80. No 2, 2018, pp. 255-266.

[28] Abuziarov M, Glazova E.G., Kochetkov A.V., Krylov S.V.. Numerical method for solving three-dimensional problems of interaction of high-speed gas jets with elastoplastic barriers. *VANT Series Mathematical modeling of physical processes*. No. 4, 2021, pp. 24-40.

[29] Barton P., Deiterding R., Meiron D., Pullin D. Eulerian adaptive finite-difference method for high-velocity impact and penetration problems, *J. Comput. Phys.*,Vol. 240, 2013, pp. 76–99.

[30] Barton P.T., Drikakis D. An Eulerian method for multi-component problems in non-linear elasticity with sliding interfaces, *J. Cornput, Phys*. Vol. 229, 2010, pp. 5518-5540.

[31] Barton P.T., Drikakis D., Romenski E. An Eulerian finite-volume scheme for large elastoplastic deformations in solids, *Int. J. Numer. Methods Eng.* Vol. 81, 2010, pp. 453-463.

[32] Schoch S., Nordin-Bates K., Nikiforakis N. An Eulerian algorithm for coupled simulations of elastoplastic solids and condensed-phase explosives, *J.Com-put. Phys*. Vol. 252, 2013, pp. 163–194.

[33] X. Zeng, C. Farhat, A systematic approach for constructing higher-order immersed boundary and ghost fluid methods for fluid and fluid-structure interaction problems, *Journal of Computational Physics,* Vol. 231, 2012, pp. 2892–2923.

[34] C. Farhat, J.F.D.R. Gerbeau, and A.Rallu. FIVER: A finite volume method based on exact two-phase Riemann problems and sparse grids for multi-material flows with large density jumps. *Journal of Computational Physics*, Vol. 231, No. 19, 2012, pp. 6360–6379.

[35] Miller G.H., Colella P. A conservative three-dimensional Eulerian method for coupled fluid-solid shock capturing, *J. Comput. Phys*. Vol. 183, 2002, pp. 26-82.

[36] Barton P.T., Obadia B., Drikakis D. A conservative level-set based method for compressible solid/fluid problems on fixed grids, *J.Comput.Phys*. Vol. 230, 2011, pp. 7867–7890.

[37] Udaykumar H.S., Tran L., Belk D.M., Vanden K.J. An Eulerian method for computation of multimatereal impact with ENO shock-capturing and sharp interfaces, *J. Comput.Phys*. Vol. 186, 2003, pp. 136–177.

[38] Barton P.T. An interface-capturing Godunov method for the simulation of compressible

solid-fluid problems, *J. Comput.Phys*. Vol. 390, 2019, pp. 25-50.

[39] Wallis Tim, T. Barton Philip, Nikiforakis Nikolaos A flux-enriched Godunov method for multi-material problems with interface slide and void opening, *Journal of Computational Physics*. Vol. 442, 2021, pp. 110499-110511.

[40] Michael L., Nikiforakis N. A multi-physics methodology for the simulation of reactive flow and elastoplastic structural response, *J.Comput.Phys*. Vol.367, 2018, pp.1–27.

[41] Favrie N., Gavrilyuk S.L., Saurel R. Solid-fluid diffuse interface model in cases of extreme deformations, *J.Comput.Phys*. Vol. 228, 2009, pp. 6037-6077.

[42] Favrie N., Gavrilyuk S.L. Diffuse interface model for compressible fluid - compressible elastic-plastic solid interaction. *J.Comput.Phys*. Vol. 231, 2012, pp. 2695-2723.

[43] Ndanou S., Favrie N., Gavrilyuk S. Multi-solid and multi-fluid diffuse interface model: applications to dynamic fracture and fragmentation, *J. Comput. Phys.* Vol. 295, 2015, pp. 523–555.

[44] Michael L., Nikiforakis N. A hybrid formulation for the numerical simulation of condensed phase explosives, *Journal of Computational Physics.* Vol. 316, 2016, pp. 193–217.

[45] Jackson Haran, Nikiforakis Nikos. A unified Eulerian framework for multimaterial continuum mechanics, *Journal of Computational Physics*. Vol. 401, 2020, pp. 109022.

[46] Adler M.C., Jain S.S., West J.R., Mani A. and Lele S.K. Diffuse-interface capturing methods for compressible multiphase fluid flows and elastic-plastic deformation in solids: *Part I. Methods, Center for Turbulence Research, Annual Research Briefs.* 2020, http://dx.doi.org/10.13140/RG.2.2.15129.65124.

[47] Wallis Tim, T. Barton Philip, Nikiforakis Nikolaos. A flux-enriched Godunov method for multi-material problems with interface slide and void opening, *Journal of Computational Physics*. Vol. 442, 2021, pp. 110499.

[48] Yashraj Bhosale, Tejaswin Parthasarathy, Mattia Gazzol A remeshed vortex method for mixed rigid/soft body fluid–structure interaction, *Journal of Computational Physics*. Vol. 444, 2021, pp. 110577.

[49] Krayukhin A.A., Stadnik L.N., Yanilkin Yu.V. Numerical simulation of the motion of rigid projectiles in elastoplastic media on a fixed computational grid using the “Egak” method, *VANT Series Mathematical modeling of physical processes*. No.1, 2019, pp. 19-32.

[50] Yanilkin Yu.V. Closure models for the equations of Lagrangian gas dynamics and elastoplastics in multicomponent cells Part 1. Isotropic models. *VANT Series Mathematical modeling of physical processes*. No.3, 2017, pp. 4-21.

[51] Yanilkin Yu.V., Toporova O.O., Kolobanin V.Yu. Closure models for the equations of Lagrangian gas dynamics and elastoplastics in multicomponent cell Part 2. Anisotropic models. *VANT Series Mathematical modeling of physical processes*. No. 3, 2017, pp. 22-38.

[52] Hank S., Favrie N., Massoni Jacques Modeling hyperelasticity in non-equilibrium multiphase flows, *J. Comput. Phys*. Vol. 330, 2017, pp. 65–91.

[53] Saurel R., Pantano C. Diffuse-interface capturing methods for compressible two-phase flows, *Annu. Rev. Fluid Mech.* Vol.50, 2018, pp. 105–130.

[54] Luis Ramírez, Xesús Nogueira, Pablo Ouro, Fermín Navarrina, Sofiane Khelladi, Ignasi Colominas. A Higher-Order Chimera Method for Finite Volume Schemes. *Archives of Computational Methods in Engineering, Springer Verlag*. Vol. 25, No.3, 2017, pp. 691-706.

[55] M.L. Wilkins, Calculation of elastic-plastic flow, in *Methods in Computational Physics*, edited by B.Alder, S.Fernbach, and M. Rotenbeg, Academic, New York, Vol. 3, pp.211-263.

[56] Abuziarov M. On the increase of the accuracy of Godunov's method for solving the problems of dynamics of gases and liquids, *XIII conference of young scientists of Moscow Physical-Technical Institute,* Vol.2. 1988, pp.30-37.

[57] Abuziarov M., Bazhenov V.G., Kochetkov A.V. On the monotonization of the Godunov

scheme of the second order of accuracy by introducing the scheme viscosity, *Applied problems of strength and plasticity. Research and optimization of structures*: 1987. pp. 85-90.

[58] Merzhievsky L.A., Paletsky. AV. Calculations for diagrams of dynamic deformation of metals and alloys. *Physical Mesomechanics*, Vol.4, No 3, pp.85-96.

[59] Piekutowski AJ, Forrestal MJ, Poormon KL, Warren TL. Perforation of aluminum plates with ogive nose steel rods at normal and oblique impacts. *Int J Impact Eng.*, Vol.18, 1996, pp. 877-887.

# Appendix 1

Godunov's scheme

$$\frac{u^i-u_i}{\Delta t}+u_0\frac{u_{i+1/2}-u_{i-1/2}}{\Delta x}+\frac{1}{\rho_0}\left(\frac{p_{i+1/2}-p_{i-1/2}}{\Delta x}\right)=0$$

$$\frac{p^i-p_i}{\Delta t}+u_0\frac{p_{i+1/2}-p_{i-1/2}}{\Delta x}+\rho_0c_0^2\left(\frac{u_{i+1/2}-u_{i-1/2}}{\Delta x}\right)=0$$

Godunov's Riemann's problem

$$u_{i-1/2}=\frac{u_{i-1}+u_i}{2}+\frac{1}{2\rho_0c_0}\left(p_{i-1}-p_i\right);$$

$$p_{i-1/2}=\frac{p_{i-1}+p_i}{2}+\frac{\rho_0c_0}{2}\left(u_{i-1}-u_i\right);$$

$$u_{i+1/2}=\frac{u_i+u_{i+1}}{2}+\frac{1}{2\rho_0c_0}\left(p_i-p_{i+1}\right);$$

$$p_{i+1/2}=\frac{p_i+p_{i+1}}{2}+\frac{\rho_0c_0}{2}\left(u_i-u_{i+1}\right);$$

Riemann's problem for this scheme

$$u_{i-1/2}=\frac{u(x_{i-1}^+)+u(x_i^-)}{2}+\frac{1}{2\rho_0c_0}\left(p(x_{i-1}^+)-p(x_i^-)\right);$$

$$p_{i-1/2}=\frac{p(x_{i-1}^+)+p(x_i^-)}{2}+\frac{\rho_0c_0}{2}\left(u(x_{i-1}^+)-u(x_i^-)\right);$$

$$u_{i+1/2}=\frac{u(x_i^+)+u(x_4)}{2}+\frac{1}{2\rho_0c_0}\left(p(x_i^+)-p(x_4)\right);$$

$$p_{i+1/2}=\frac{p(x_i^+)+p(x_{i+1}^-)}{2}+\frac{\rho_0c_0}{2}\left(u(x_i^+)-u(x_{i+1}^-)\right);$$

# Appendix 2

$$\frac{u^i-u_i}{\Delta t}=u_t+\frac{1}{2}u_{tt}\Delta t+\bar{o}\left(\Delta t^2\right)$$

$$\frac{p^i-p_i}{\Delta t}=p_t+\frac{1}{2}p_{tt}\Delta t+\bar{o}\left(\Delta t^2\right)$$

$u_{tt}+u_0*u_{xt}+\frac{1}{\rho_0}*p_{xt}=0;\quad \frac{\partial}{\partial t}$ of the first eq. of sys.6

$p_{tt}+u_0*p_{xt}+\rho_0c_0^2*u_{xx}=0;\quad \frac{\partial}{\partial t}$ of the second eq. of sys.6

$u_{tx}+u_0*u_{xx}+\frac{1}{\rho_0}*p_{xx}=0;\quad \frac{\partial}{\partial x}$ of the first eq. of sys.6

$p_{tx}+u_0*p_{xx}+\rho_0c_0^2*u_{xx}=0;\quad \frac{\partial}{\partial x}$ of the second eq. of sys.6

$$\Rightarrow u_{tt}=2\frac{u_0}{\rho_0}p_{xx}+\left(u_0^2+c_0^2\right)u_{xx}$$

$$\Rightarrow \frac{u^i-u_i}{\Delta t}=u_t+\frac{\Delta t}{2}\left(2\frac{u_0}{\rho_0}p_{xx}+\left(u_0^2+c_0^2\right)u_{xx}\right)+\bar{o}\left(\Delta t^2\right)$$

$$\Rightarrow p_{tt}=2u_0\rho_0c_0^2u_{xx}+\left(u_0^2+c_0^2\right)p_{xx}$$

$$\Rightarrow \frac{p^i-p_i}{\Delta t}=p_t+\frac{\Delta t}{2}\left(2u_0\rho_0c_0^2u_{xx}+\left(u_0^2+c_0^2\right)p_{xx}\right)+\bar{o}\left(\Delta t^2\right)$$

$$p(x_{i-1}^+)=p(x_i)-\frac{p(x_i)-p(x_{i-1})}{\left(h_{i-1}+h_i\right)/2}\left(h_i/2-x_{i-1}^+\right)=$$

$$=p(x_i)-\frac{p(x_i)-\left[p(x_i)-p_x(x_i)\frac{h_{i-1}+h_i}{2}+p_{xx}(x_i)\frac{(h_{i-1}+h_i)^2}{2*4}+\bar{o}(h_i^2)\right]}{\left(h_{i-1}+h_i\right)/2}\left(h_i/2-x_{i-1}^+\right)$$

$$p(x_{i-1}^+)=p(x_i)-p_x(x_i)\left(h_i/2-x_{i-1}^+\right)+\frac{1}{2}p_{xx}(x_i)\left(h_{i-1}+h_i\right)/2\left(h_i/2-x_{i-1}^+\right)+\bar{o}(h_i^2)$$

$$u(x_{i-1}^+)=u(x_i)-u_x(x_i)\left(h_i/2-x_{i-1}^+\right)+\frac{1}{2}u_{xx}(x_i)\left(h_{i-1}+h_i\right)/2\left(h_i/2-x_{i-1}^+\right)+\bar{o}(h_i^2)$$

$$p(x_i^-)=p(x_i)-p_x(x_i)\left(h_i/2-x_i^-\right)+\frac{1}{2}p_{xx}(x_i)\left(h_{i-1}+h_i\right)/2\left(h_i/2-x_i^-\right)+\bar{o}(h_i^2)$$

$$u(x_i^-)=u(x_i)-u_x(x_i)\left(h_i/2-x_i^-\right)+\frac{1}{2}u_{xx}(x_i)\left(h_{i-1}+h_i\right)/2\left(h_i/2-x_i^-\right)+\bar{o}(h_i^2)$$

$$p(x_i^+)=p(x_i)+p_x(x_i)\left(h_i/2+x_i^+\right)+\frac{1}{2}p_{xx}(x_i)\left(h_i+h_{i+1}\right)/2\left(h_i/2+x_i^+\right)+\bar{o}(h_i^2)$$

$$u(x_i^+)=u(x_i)+u_x(x_i)\left(h_i/2+x_i^+\right)+\frac{1}{2}u_{xx}(x_i)\left(h_i+h_{i+1}\right)/2\left(h_i/2+x_i^+\right)+\bar{o}(h_i^2)$$

$$p(x_{i+1}^-)=p(x_i)+p_x(x_i)\left(h_i/2+x_{i+1}^-\right)+\frac{1}{2}p_{xx}(x_i)\left(h_i+h_{i+1}\right)/2\left(h_i/2+x_{i+1}^-\right)+\bar{o}(h_i^2)$$

$$u(x_{i+1}^-)=u(x_i)+u_x(x_i)\left(h_i/2+x_{i+1}^-\right)+\frac{1}{2}u_{xx}(x_i)\left(h_i+h_{i+1}\right)/2\left(h_i/2+x_{i+1}^-\right)+\bar{o}(h_i^2)$$

**Contribution of Individual Authors to the Creation of a Scientific Article (Ghostwriting Policy)**

The authors equally contributed to the present research, at all stages from the formulation of the problem to the final findings and solution.

**Sources of Funding for Research Presented in a Scientific Article or Scientific Article Itself**

This work has been supported by the grants of the Russian Science Foundation, RSF 22-79-10076.

**Conflict of Interest**

The authors have no conflicts of interest to declare.